International Journal of Non-Linear Mechanics 127 (2020) 103575

Contents lists available at ScienceDirect

International Journal of Non-Linear Mechanics

journal homepage: www.elsevier.com/locate/nlm

Nonlinear analysis of functionally graded beams using the dual mesh finite domain method and the finite element method

J.N. Reddy *, Praneeth Nampally, Arun R. Srinivasa

J. Mike Walker'66 Department of Mechanical Engineering, Texas A&M University, College Station, TX 77843-3123, USA

ARTICLE INFO

Keywords:
Dual mesh finite domain method
The finite element method
Functionally graded beams
Displacement and mixed models
Nonlinear analysis
Numerical results

ABSTRACT

In this paper, geometrically nonlinear analysis of functionally graded beams using the *dual mesh finite domain method* (DMFDM) and the finite element method is presented. The DMFDM makes use of a primal mesh of finite elements and associated approximation for the variables of the formulation and a dual mesh of control domains, which does not overlap the primal mesh, for the satisfaction of the governing equations. The dual variables can be postcomputed uniquely and accurately at the control domain interfaces. The method is used to obtain nonlinear (due to the von Kármán nonlinear strains) bending solutions of straight, through-thickness functionally graded beams using the Euler–Bernoulli and the Timoshenko beam theories. Mixed models, which contain displacements and the bending moment as degrees of freedom, and displacement models are developed. Numerical results of linear and nonlinear analyses are presented to illustrate the methodology and a comparison of the generalized displacements and bending moments obtained with the DMFDM and FEM models while bringing out certain interesting features of functionally graded beams.

1. Introduction

1.1. Background

Numerical simulation of physical phenomena has dominated engineering research and practice for the last several decades. Computational engineering science — a phrase that is used for numerical simulations of a variety of physical systems, is responsible for the remarkable advances in transportation, communication, materials processing, manufacturing, medicine, and biotechnology. The finite element method (FEM), a compute-oriented technique of solving differential equations [1,2], has emerged as a versatile and powerful analysis tool, and today it is the most commonly used computational platform in a variety of industries. Despite its popularity in solid and structural mechanics field since early 1970's, the method has not been able to compete with the finite volume method (FVM) in computational fluid dynamics applications [3–5]. This is largely due to two drawbacks of the FEM. First, the unique feature of the FEM, namely representing a system as a collection of connected subsystems, often results in discontinuous representation of the secondary (force-like) variables. Second, the weak-form Galerkin formulations, which satisfy the governing differential equations in a weighted-integral sense, has the tendency to smoothen the solution and thereby predicts a diffuse solution.

In the FVM the governing differential equations are satisfied an integral (not a weighted-integral) to derive the discretized equations. The algebraic equations derived using a typical control volume involve mesh point values from the neighboring control volumes (a notable difference from FEM, where discrete equations are solely in terms of the element degrees of freedom), and thereby naturally connecting the control volumes without discontinuity of the variable or its dual. However, the FVM also suffers from two drawbacks. First, there is no explicit representation of the solution variables, making integration of the expressions involving the variables arbitrarily evaluated. Second, there is no unique methodology exists for the imposition of gradient boundary conditions. The major advantage of the FVM is that they satisfy the global form of the governing equations exactly.

Noting the limitations of the two most popular numerical methods, Reddy [6] introduced a numerical approach termed the *dual mesh finite domain method* (DMFDM) that uses the best features of the FEM and FVM. In the DMFDM, the domain is represented with a mesh of finite elements and a dual mesh is superimposed on the primal mesh such that the nodes of the primal mesh are at the center of the dual mesh of finite domains, except for the nodes on the boundary. Then the governing equation is required to be satisfied in an integral sense over the finite (control) domain. The second-order terms in the differential equation are integrated-by-parts and expressed as dual variables on the interfaces of the dual mesh. When the interfaces fall on the boundary, either the dual variables or their counterparts (i.e., primary variables) are known. The approach, by very construction of the discretization procedure, does not involve isolating a finite element and satisfying

* Corresponding author.
E-mail address: jnreddy@tamu.edu (J.N. Reddy).

https://doi.org/10.1016/j.ijnonlinmec.2020.103575
Received 1 July 2020; Received in revised form 3 August 2020; Accepted 4 August 2020
Available online 24 August 2020
0020-7462/© 2020 Elsevier Ltd. All rights reserved.

the governing equations in weak sense (i.e., weighted-integral sense) over the element and assembling element equations to obtain the global equations. Instead, the DMFDM results directly in a set of global equations in terms of the nodal values of the primary variables. Thus, the DMFDM brings the best features of the FEM and the FVM and *makes use of the duality concept to implement physical boundary conditions*. The method is recently applied to single-variable linear differential equations in one and two dimensions in [6] and to linear bending of beams in [7].

1.2. The present study

In this paper, the DMFDM is extended to nonlinear differential equations with multiple variables. In particular, we consider nonlinear bending of functionally graded beams using the Euler–Bernoulli beam theory (EBT) and the Timoshenko beam theory (TBT). The governing equations are reformulated as second-order equations to facilitate the application of the DMFDM. This naturally requires, in the case of the EBT, to reformulate the fourth-order differential equation in terms of the deflection and bending moment. Thus, mixed models of the nonlinear equations of the FGM beams according to the EBT as well as TBT are developed, and numerical examples are presented to illustrate the application of the DMFDM to nonlinear problems. Numerical results obtained with the DMFDM models are compared with those obtained using the finite element models (displacement as well as mixed) to assess the relative accuracy of both the primary variables (generalized displacements) and the secondary variables (generalized forces).

Following this introduction, a review of the governing equations of the Euler–Bernoulli and Timoshenko beam theories (see Reddy [8] and Reddy and Srinivasa [9]) as applied to nonlinear bending of functionally graded beams is presented in Section 2. Here two sets of equations, one in terms of the generalized displacements and the other in terms of the generalized displacements and bending moment are developed as they are not readily available in the literature (see Reddy and Nampally [7] for the linear case). The dual mesh finite domain discretizations of the three models, namely, mixed model of the EBT, mixed model of the TBT, and the displacement model of the TBT are presented in Section 3. Then, in Section 4, numerical results for the generalized displacements and generalized forces are presented for various boundary conditions and loads. Finally, some remarks about the DMFDM and its extensions are outlined in Section 5.

2. A review of beam theories

2.1. Functionally graded beams

Here we consider beams in which the two different material are combined in a predetermined fashion to vary through the beam thickness (only), while they remain the same along the length of the beam (see, for example, [10–13]). The basic idea of gradation of material properties through the thickness is to construct beam structures that exhibit desired structural properties (e.g., thermal resistance, fracture toughness, etc.) while avoiding abrupt change of material properties (like in the layered beams), which produce residual stresses and stress concentrations. Also, if two dissimilar materials are bonded together, there is a very high chance that debonding will occur at the interface. These problems can be resolved by gradually varying the volume fraction of the constituents selected rather than abruptly changing them over an interface. The gradual variation results in a very efficient material tailored to suit the functionality of the structure.

A two-constituent functionally graded through-thickness materials are characterized by a power-law variation of modulus of elasticity while the Poisson ratio is kept constant. If the x-axis is taken along the length of the beam and the z-coordinate is taken along the thickness (the height) of the beam, the modulus $E(z)$ of an FGM beam is assumed to be represented by the simple power-law as (see Praveen and Reddy [11] and Reddy [14])

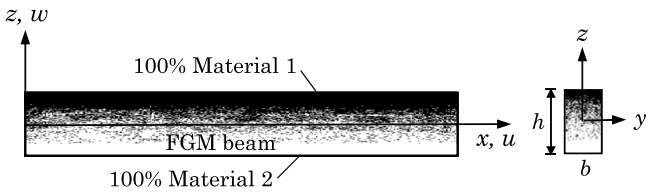

Fig. 1. Geometry of a through-thickness functionally graded beam.

$$E(z) = \left(E_1 - E_2\right) f(z) + E_2, \quad f(z) = \left(\frac{1}{2} + \frac{z}{h}\right)^n \tag{1}$$

where E_1 and E_2 are the material properties of material 1 (at the top) and material 2 (at the bottom face), respectively (see 1), and n is the power-law index. Note that when $n = 0$, we obtain the single-material structure (with modulus E_1).

2.2. The Euler–Bernoulli beam theory (EBT)

The equations of equilibrium of the EBT, accounting for the von Kármán nonlinear strain to account for moderate rotations, are given by (see Reddy [8]):

$$-\frac{dN_{xx}}{dx} - f = 0 \tag{2a}$$

$$-\frac{d^2M_{xx}}{dx^2} - \frac{d}{dx}\left(N_{xx}\frac{dw}{dx}\right) + c_f w - q = 0 \tag{2b}$$

where $f(x)$ and $q(x)$ axial and transverse distributed loads, respectively, on the beam, c_f is the modulus of the foundation on which the beam rests, and N_{xx} and M_{xx} are the stress resultants defined by (and expressed in terms of the generalized displacements u and w, with $\theta_x = -dw/dx$):

$$N_{xx} = \int_A \sigma_{xx}\, dA = A_{xx}\varepsilon_{xx}^{(0)} + B_{xx}\varepsilon_{xx}^{(1)} \tag{3a}$$

$$M_{xx} = \int_A z\sigma_{xx}\, dA = B_{xx}\varepsilon_{xx}^{(0)} + D_{xx}\varepsilon_{xx}^{(1)} \tag{3b}$$

Here $\varepsilon_{xx}^{(0)}$ and $\varepsilon_{xx}^{(1)}$ denote the membrane and bending strains,

$$\varepsilon_{xx}^{(0)}(x) = \frac{du}{dx} + \frac{1}{2}\left(\frac{dw}{dx}\right)^2, \quad \varepsilon_{xx}^{(1)}(x) = -\frac{d^2w}{dx^2} \tag{4}$$

and A_{xx}, B_{xx}, and D_{xx} are the extensional, extensional-bending, and bending stiffness coefficients

$$(A_{xx}, B_{xx}, D_{xx}) = \int_A (1, z, z^2) E(z)\, dA \tag{5}$$

The form of the associated duality pairs are: (u, N_{xx}), (w, V_x), and (θ_x, M_{xx}), where

$$V_x \equiv \frac{dM_{xx}}{dx} + N_{xx}\frac{dw}{dx} \tag{6}$$

We remark that there are two sources of coupling between the axial displacement u and the transverse displacement w in FGM beams: first, the coupling is due to the extensional-bending coefficient B_{xx}, and it is independent of the von Kármán nonlinear strain term; second, the coupling is due to the von Kármán nonlinearity, which is independent of the coupling coefficient B_{xx}. Of course, the coefficient B_{xx} has a stronger coupling in the presence of the von Kármán nonlinearity.

Eq. (2b), when expressed in terms of the displacement w, results in a fourth-order differential equation, which is not suitable for the application of the DMFDM. Therefore, we reformulate the governing equations as second-order differential equations in terms of (u, w, M_{xx}).

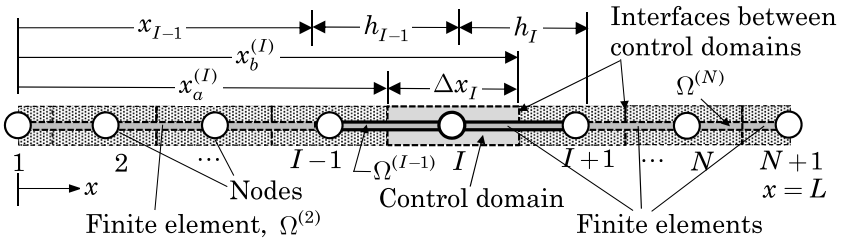

Fig. 2. A primal mesh of finite elements and dual mesh of control domains. We note that the boundary nodes have only half control domains whereas the internal nodes have full control domains. Also, each control domain connects two neighboring finite elements (one on the left and the other on the right) and thus automatic assembly of element equations takes place.

Substitution of Eqs. (3a) and (3b) into Eqs. (2a) and (2b) gives the following governing equations in terms of the displacements:

$$-\frac{d}{dx}\left\{\bar{A}_{xx}\left[\frac{du}{dx}+\frac{1}{2}\left(\frac{dw}{dx}\right)^2\right]+\bar{B}_{xx}M_{xx}\right\}=f \tag{7a}$$

$$-\frac{d^2M_{xx}}{dx^2}-\frac{d}{dx}\left\{\bar{A}_{xx}\frac{dw}{dx}\left[\frac{du}{dx}+\frac{1}{2}\left(\frac{dw}{dx}\right)^2\right]+\bar{B}_{xx}\frac{dw}{dx}M_{xx}\right\}+c_f w=q \tag{7b}$$

$$-\frac{d^2w}{dx^2}-\frac{M_{xx}}{D_{xx}}+\bar{B}_{xx}\left[\frac{du}{dx}+\frac{1}{2}\left(\frac{dw}{dx}\right)^2\right]=0 \tag{7c}$$

where

$$D^*_{xx}\equiv D_{xx}A_{xx}-B^2_{xx},\quad \bar{A}_{xx}\equiv\frac{D^*_{xx}}{D_{xx}},\quad \bar{B}_{xx}\equiv\frac{B_{xx}}{D_{xx}} \tag{8}$$

We note that, for the nonlinear FGM beams, the axial force N_{xx} is expressed in terms of the displacements (u,w) and moment (M_{xx}) as

$$N_{xx}=\bar{A}_{xx}\left[\frac{du}{dx}+\frac{1}{2}\left(\frac{dw}{dx}\right)^2\right]+\bar{B}_{xx}M_{xx} \tag{9}$$

2.3. The Timoshenko beam theory (TBT)

The equations of equilibrium of the Timoshenko beam theory are

$$-\frac{dN_{xx}}{dx}-f=0 \tag{10a}$$

$$-\frac{dQ_x}{dx}-\frac{d}{dx}\left(N_{xx}\frac{dw}{dx}\right)+c_f w-q=0 \tag{10b}$$

$$-\frac{dM_{xx}}{dx}+Q_x=0 \tag{10c}$$

The stress resultants (N_{xx},M_{xx},Q_x) in the TBT can be expressed in terms of the displacements as

$$N_{xx}=A_{xx}\left[\frac{du}{dx}+\frac{1}{2}\left(\frac{dw}{dx}\right)^2\right]+B_{xx}\frac{d\phi_x}{dx} \tag{11a}$$

$$M_{xx}=B_{xx}\left[\frac{du}{dx}+\frac{1}{2}\left(\frac{dw}{dx}\right)^2\right]+D_{xx}\frac{d\phi_x}{dx} \tag{11b}$$

$$Q_x=K_s\int_A\sigma_{xz}\,dA=S_{xz}\left(\phi_x+\frac{dw}{dx}\right) \tag{11c}$$

where ϕ_x denotes the rotation of the cross section about the y-axis, K_s the shear correction factor, and S_{xz} is the shear stiffness coefficient

$$S_{xz}=\frac{K_s}{2(1+\nu)}\int_A E(z)\,dA \tag{12}$$

The governing equations of the TBT are second order and can be discretized using the DMFDM. To have a mixed model for comparison with its EBT counterpart, we shall also develop equations suitable for the mixed formulation of the TBT in terms of (u,w,M_{xx}) (i.e., eliminate ϕ_x). The resulting equations are

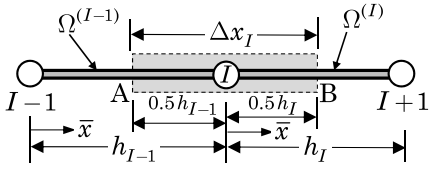

Fig. 3. Control domain associated with an interior node I. We note that each node has three unknowns and the control domain connects nine nodal values $(U_{I-1},W_{I-1},M_{I-1})$, (U_I,W_I,M_I), and $(U_{I+1},W_{I+1},M_{I+1})$ through the discretization of three governing equations.

$$-\frac{d}{dx}\left\{\bar{A}_{xx}\left[\frac{du}{dx}+\tfrac{1}{2}\left(\frac{dw}{dx}\right)^2\right]+\bar{B}_{xx}M_{xx}\right\}=f \tag{13a}$$

$$-\frac{d^2M_{xx}}{dx^2}-\frac{d}{dx}\left\{\bar{A}_{xx}\frac{dw}{dx}\left[\frac{du}{dx}+\tfrac{1}{2}\left(\frac{dw}{dx}\right)^2\right]+\bar{B}_{xx}\frac{dw}{dx}M_{xx}\right\}+c_f w=q \tag{13b}$$

$$-\frac{d}{dx}\left[\frac{dw}{dx}-\frac{1}{S_{xz}}\frac{dM_{xx}}{dx}\right]+\bar{B}_{xx}\left[\frac{du}{dx}+\tfrac{1}{2}\left(\frac{dw}{dx}\right)^2\right]-\frac{1}{D_{xx}}M_{xx}=0 \tag{13c}$$

where the effective rotation $\hat{\phi}_x$ is

$$\hat{\phi}_x=-\frac{dw}{dx}+\frac{1}{S_{xz}}\frac{dM_{xx}}{dx} \tag{14}$$

The displacement finite element models of the EBT and TBT are available in the book by Reddy [2]. The mixed models of the EBT and TBT for the FGM beams are not readily available; therefore they are listed in Appendix.

3. Discretized equations using the DMFDM

3.1. The mixed Euler–Bernoulli beam model

The DMFDM is best suited to discretize second-order equations. Therefore, we can only consider the mixed model of the EBT using Eqs. (7a)–(7c). The domain $\Omega=(0,L)$ divided into a set of N finite elements (can be a nonuniform mesh) separated by nodes, as shown in Fig. 2, with each node having its own finite domain (a dual mesh) around it. The first and last nodes have half control domains. The nodes and elements are numbered sequentially from the left to the right. We consider a typical interior node I and the control domain associated with that node (see Fig. 3) to discretize the equations.

In order to derive the discretized equations, we write the integral statements of Eqs. (7a)–(7c) over the control domain and carry out integration-by-parts of expressions which contain the second differential; that is, unlike in a weighted-residual method (or weak form), we

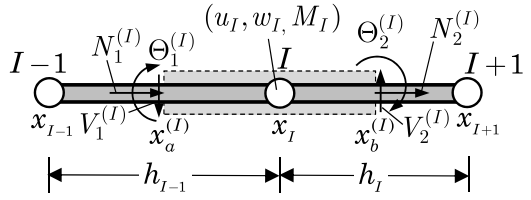

Fig. 4. A typical control domain for the mixed model of the EBT.

weaken the differentiability by carrying out the integration-by-parts. For example, considering Eq. (7a), we obtain

$$\begin{aligned} 0 &= \int_A^B \left\{ -\frac{d}{dx}\left[\bar{A}_{xx}\left(\frac{du}{dx} + \tfrac{1}{2}\left(\frac{dw}{dx}\right)^2 \right) + \bar{B}_{xx} M_{xx} \right] - f \right\} dx \\ &= \left[\bar{A}_{xx}\left(\frac{du}{dx} + \tfrac{1}{2}\left(\frac{dw}{dx}\right)^2 \right) + \bar{B}_{xx} M_{xx} \right]_{x_a^{(I)}} \\ &\quad - \left[\bar{A}_{xx}\left(\frac{du}{dx} + \tfrac{1}{2}\left(\frac{dw}{dx}\right)^2 \right) + \bar{B}_{xx} M_{xx} \right]_{x_b^{(I)}} \\ &\quad - \int_{x_a^{(I)}}^{x_b^{(I)}} f\, dx \end{aligned} \tag{15}$$

or

$$0 = -N_1^{(I)} - N_2^{(I)} - \int_{x_a^{(I)}}^{x_b^{(I)}} f\, dx \tag{16a}$$

where

$$N_1^{(I)} \equiv -\left[\bar{A}_{xx}\left(\frac{du}{dx} + \tfrac{1}{2}\left(\frac{dw}{dx}\right)^2 \right) + \bar{B}_{xx} M_{xx} \right]_{x_a^{(I)}} \tag{16b}$$

$$N_2^{(I)} \equiv \left[\bar{A}_{xx}\left(\frac{du}{dx} + \tfrac{1}{2}\left(\frac{dw}{dx}\right)^2 \right) + \bar{B}_{xx} M_{xx} \right]_{x_b^{(I)}} \tag{16c}$$

Here points A and B refer to the left and right end locations of the control domain (associated with node I), which have the coordinates $x_a^{(I)}$ and $x_b^{(I)}$, respectively (note that point A is in element $\Omega^{(I-1)}$ and point B is in element $\Omega^{(I)}$; see Fig. 3); $N_1^{(I)}$ and $N_2^{(I)}$ denote the secondary variables (in the present case, they are the axial forces) at the left and right interfaces of the control domain centered at node I (see Fig. 4 for the nodal degrees of freedom). The minus sign in the definition of $N_1^{(I)}$ indicates that it is a compressive force; both $N_1^{(I)}$ and $N_2^{(I)}$ are axial forces in the positive x direction.

Similarly, Eq. (7b) takes the form

$$0 = -V_1^{(I)} - V_2^{(I)} + \int_{x_a^{(I)}}^{x_b^{(I)}} (c_f w - q)\, dx \tag{17a}$$

where $V_1^{(I)}$ and $V_2^{(I)}$ denote the secondary variables (shear forces acting upward positive) at the left and right interfaces of the control domain centered at node I,

$$V_1^{(I)} \equiv -\left[\frac{dM}{dx} + N_{xx}\frac{dw}{dx} \right]_{x_a^{(I)}}, \quad V_2^{(I)} \equiv \left[\frac{dM}{dx} + N_{xx}\frac{dw}{dx} \right]_{x_b^{(I)}} \tag{17b}$$

and N_{xx} is known in terms of the displacements (u, w) and bending moment M_{xx} through Eq. (9).

The integral statement associated with Eq. (7c) is

$$0 = -\Theta_1^{(I)} + \Theta_2^{(I)} + \int_{x_a^{(I)}}^{x_b^{(I)}} \left[-\frac{1}{D_{xx}} M_{xx} + \bar{B}_{xx}\left(\frac{du}{dx} + \tfrac{1}{2}\left(\frac{dw}{dx}\right)^2 \right) \right] dx \tag{18a}$$

where $\Theta_1^{(I)}$ and $\Theta_2^{(I)}$ denote the secondary variables (rotations in counterclockwise direction) at the left and right interfaces of the control domain centered at node I,

$$\Theta_1^{(I)} \equiv \left[-\frac{dw}{dx} \right]_{x_a^{(I)}}, \quad \Theta_2^{(I)} \equiv \left[-\frac{dw}{dx} \right]_{x_b^{(I)}} \tag{18b}$$

To complete the discretization, we invoke the finite element approximations of (u, w, M_{xx}) over a typical finite element $\Omega^{(I)} = (x_I, x_{I+1})$. Here we use equal degree (Lagrange) interpolation of all three variables. For example, the finite element approximation of $u(x)$ over $\Omega^{(I)}$ is

$$u(\bar{x}) \approx U_I \psi_1^{(I)}(\bar{x}) + U_{I+1}\psi_2^{(I)}(\bar{x}) \tag{19}$$

where U_I is the value of u at node I (i.e., $U_I \approx u(x_I)$) and $\psi_i^{(I)}(\bar{x})$ $(i = 1, 2)$ are linear finite element interpolation functions of element $\Omega^{(I)}$ for $I = 1, 2, \ldots, N$ written in terms of the local coordinate $\bar{x}$ ($\bar{x}$ has its origin at the left node of each finite element; see Fig. 5):

$$\psi_1^{(I)}(\bar{x}) = 1 - \frac{\bar{x}}{h_I}, \quad \psi_2^{(I)}(x) = \frac{\bar{x}}{h_I} \tag{20}$$

Hence, we can calculate the $(N_1^{(I)}, N_2^{(I)})$ in Eqs. (16b) and (16c), $(V_1^{(I)}, V_2^{(I)})$ in Eq. (17b), and $(\Theta_1^{(I)}, \Theta_2^{(I)})$ in Eq. (18b) in terms of the nodal values of (u, w, M_{xx}) using the interpolation of the type in Eq. (19) for each of the dependent variable of the formulation, while linearizing the nonlinear terms.

The linearization is a necessary to be able to solve the final algebraic equations resulting from the application of a numerical method to differential equations. The final algebraic equations (which are nonlinear if the differential equations are nonlinear) obtained with the FEM, FVM, or DMFDM has the form

$$\mathbf{K}(\boldsymbol{\Delta})\boldsymbol{\Delta} = \mathbf{F} \tag{21}$$

where $\mathbf{K}$ is the coefficient matrix (known in terms of $\boldsymbol{\Delta}$), $\boldsymbol{\Delta}$ is the column vector of nodal unknowns, and $\mathbf{F}$ is the source vector (known). Eq. (21) is solved using a successive approximation known as the direct iteration method or the Picard iteration method. Suppose that we are at the end of the rth iteration and seeking the $(r+1)$st iteration solution. Then we have

$$\mathbf{K}(\boldsymbol{\Delta}^r)\boldsymbol{\Delta}^{r+1} = \mathbf{F} \quad \rightarrow \quad \boldsymbol{\Delta}^{r+1} = (\mathbf{K}^r)^{-1}\mathbf{F} \tag{22}$$

where $\mathbf{K}^r \equiv \mathbf{K}(\boldsymbol{\Delta}^r)$. The iteration is continued until the difference between two consecutive solutions (measured with a suitable measure) is within a prescribed tolerance:

$$\sqrt{\frac{\delta\boldsymbol{\Delta}\cdot\delta\boldsymbol{\Delta}}{\boldsymbol{\Delta}^r\cdot\boldsymbol{\Delta}^r}} \le \epsilon, \quad \delta\boldsymbol{\Delta} \equiv \boldsymbol{\Delta}^{r+1} - \boldsymbol{\Delta}^r \tag{23}$$

where ϵ denotes a preselected value of the error tolerance (say, $\epsilon = 10^{-3}$). In the beginning of the iteration, one must have a starting guess vector $\boldsymbol{\Delta}^0$; in the case of structural problems, we can take the initial guess vector to be zero so that the first iteration solution is the linear solution.

In the present case, the linearization amounts to calculating the nonlinear terms using the previous iteration solution. For example, we can linearize $(dw/dx)^2$ and $(dw/dx)^3$ as

$$\left(\frac{dw}{dx}\right)^2 \approx \left[\frac{dw}{dx}\right]^r \frac{dw}{dx}; \quad \left(\frac{dw}{dx}\right)^3 \approx \left[\left(\frac{dw}{dx}\right)^2\right]^r \frac{dw}{dx}$$

where the term in the square bracket is evaluated using the known solution from the rth iteration.

Discretization of Eq. (7a)

Returning to the DMFDM discretization of Eq. (16a), we first express $(N_1^{(I)}, N_2^{(I)})$ in Eqs. (16b) and (16c) in terms of the nodal values of the primary variables:

$$N_1^{(I)} = -\bar{A}_{I-1}\frac{U_I - U_{I-1}}{h_{I-1}} - \tfrac{1}{2}\bar{A}_{I-1}\Delta W_{I-1}\frac{W_I - W_{I-1}}{h_{I-1}} - \bar{B}_{I-1}\frac{M_{I-1} + M_I}{2} \tag{24a}$$

$$N_2^{(I)} = \bar{A}_I\frac{U_{I+1} - U_I}{h_I} + \tfrac{1}{2}\bar{A}_I\Delta W_I\frac{W_{I+1} - W_I}{h_I} + \bar{B}_I\frac{M_I + M_{I+1}}{2} \tag{24b}$$

where $\bar{A}_{I-1} = \bar{A}_{xx}(x_a^{(I)})$ at the left interface and $\bar{A}_I = \bar{A}_{xx}(x_b^{(I)})$ at the right interface of the finite domain centered around node I. Similar meaning applies to $\bar{B}_{I-1}$ and $\bar{B}_I$; W_I and M_I denote the nodal values

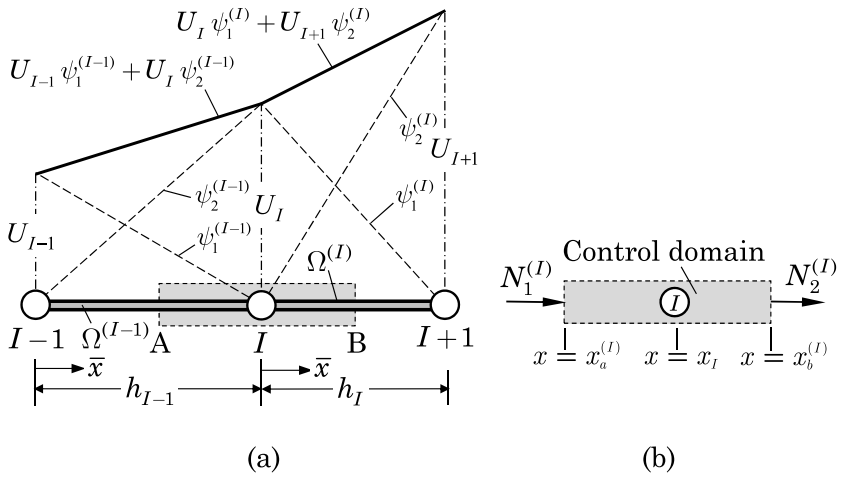

Fig. 5. Linear finite element approximation over a control domain.

of w and M_{xx}, respectively, at node I, while ΔW_I denotes the value of dw/dx in element $\Omega^{(I)}$, based on the previous iteration solution.

Substituting the approximations (24a) and (24b) into Eq. (16a), we obtain (for $I = 2, 3, \ldots, N$)

$$
\begin{aligned}
&-\frac{\bar{A}_{I-1}}{h_{I-1}}U_{I-1} + \left(\frac{\bar{A}_{I-1}}{h_{I-1}} + \frac{\bar{A}_I}{h_I}\right)U_I - \frac{\bar{A}_I}{h_I}U_{I+1} \\
&+ 0.5\left[-\frac{\bar{A}_{I-1}\Delta W_{I-1}}{h_{I-1}}W_{I-1} + \left(\frac{\bar{A}_{I-1}\Delta W_{I-1}}{h_{I-1}} + \frac{\bar{A}_I\Delta W_I}{h_I}\right)W_I - \frac{\bar{A}_I\Delta W_I}{h_I}W_{I+1}\right] \\
&+ 0.5\bar{B}_{I-1}M_{I-1} + 0.5\left(\bar{B}_{I-1} - \bar{B}_I\right)M_I - 0.5\bar{B}_I M_{I+1} - F_I = 0
\end{aligned} \tag{25}
$$

where

$$
\bar{A}_{I-1} = \left.\frac{D^*_{xx}}{D_{xx}}\right|_{x_a^{(I)}},\quad \bar{A}_I = \left.\frac{D^*_{xx}}{D_{xx}}\right|_{x_b^{(I)}},\quad \bar{B}_{I-1} = \left.\frac{B_{xx}}{D_{xx}}\right|_{x_a^{(I)}},\quad \bar{B}_I = \left.\frac{B_{xx}}{D_{xx}}\right|_{x_b^{(I)}}
$$

$$
\Delta W_{I-1} = \frac{\bar{W}_I - \bar{W}_{I-1}}{h_{I-1}},\quad \Delta W_I = \frac{\bar{W}_{I+1} - \bar{W}_I}{h_I},\quad F_I = \int_{x_a^{(I)}}^{x_b^{(I)}} f(x)\,dx \tag{26}
$$

Here $\bar{W}_I$ denotes the value of w at node I from the previous iteration to solve the nonlinear algebraic equations. The integral of a function f over the control domain $(x_a^{(I)}, x_b^{(I)})$ can be evaluated using either exact integration or numerical integration (e.g., one-third Simpson's rule).

Next, we should obtain the discretized equation for the boundary nodes, node 1 and node $N+1$ (when there are N linear elements in the primal mesh). We note that at node 1, $N_1^{(1)}$ is the boundary axial force, which is known or its dual, U_1, is known. Hence, we only evaluate $N_2^{(1)}$ at $h_1/2$. The discretized equations of the left boundary node is [see Fig. 6(a)]

$$
\begin{aligned}
0 &= -N_1^{(1)} - \bar{A}_1\frac{U_2 - U_1}{h_1} - 0.5\bar{A}_1\,\Delta W_1\frac{W_2 - W_1}{h_1} - \bar{B}_1\frac{M_2 + M_1}{2} - \int_0^{0.5h_1} f\,dx \\
&= -N_1^{(1)} + \frac{\bar{A}_1}{h_1}U_1 - \frac{\bar{A}_1}{h_1}U_2 + 0.5\frac{\bar{A}_1\,\Delta W_1}{h_1}W_1 - 0.5\frac{\bar{A}_1\,\Delta W_1}{h_1}W_2 \\
&\quad - 0.5\bar{B}_1\,M_1 - 0.5\bar{B}_1\,M_2 - \int_0^{0.5h_1} f\,dx
\end{aligned} \tag{27}
$$

Similarly, for the node on the right boundary [see Fig. 6(b)], we have

$$
\begin{aligned}
0 &= -N_2^{(N+1)} - \frac{\bar{A}_N}{h_N}U_N + \frac{\bar{A}_N}{h_N}U_{N+1} - 0.5\frac{\bar{A}_N\,\Delta W_N}{h_N}W_N + 0.5\frac{\bar{A}_N\,\Delta W_N}{h_N}U_{N+1} \\
&\quad + 0.5\bar{B}_N\,M_N + 0.5\bar{B}_N\,M_{N+1} - \int_0^{0.5h_N} f\,d\bar{x}
\end{aligned} \tag{28}
$$

This completes the discretization of Eq. (7a).

Discretization of Eq. (7b)

The same procedure can be applied to Eq. (7b) to obtain the discretized equations for the interior and boundary nodes. Discretized values of $(V_1^{(I)}, V_2^{(I)})$ are

$$
\begin{aligned}
V_1^{(I)} &= -\frac{M_I - M_{I-1}}{h_{I-1}} - \bar{A}_{I-1}\Delta W_{I-1}\frac{U_I - U_{I-1}}{h_{I-1}} - 0.5\bar{A}_{I-1}(\Delta W)^2_{I-1}\frac{W_I - W_{I-1}}{h_{I-1}} \\
&\quad - 0.5\left[\bar{B}_{I-1}\,\Delta W_{I-1}\left(M_{I-1} + M_I\right)\right]
\end{aligned} \tag{29a}
$$

$$
\begin{aligned}
V_2^{(I)} &= \frac{M_{I+1} - M_I}{h_I} + \bar{A}_I\,\Delta W_I\frac{U_{I+1} - U_I}{h_I} + 0.5\bar{A}_I\,(\Delta W)^2_I\frac{W_{I+1} - W_I}{h_I} \\
&\quad + 0.5\left[\bar{B}_I\Delta W_I\left(M_I + M_{I+1}\right)\right]
\end{aligned} \tag{29b}
$$

The integral of $c_f\,w$ over the control domain $(x_a^{(I)}, x_b^{(I)})$, for the linear interpolation used, is

$$
\int_{x_a^{(I)}}^{x_b^{(I)}} c_f w\,dx = \frac{1}{8}\left[C_{I-1}W_{I-1}h_{I-1} + 3W_I\left(C_{I-1}h_{I-1} + C_I h_I\right) + C_I W_{I+1}h_I\right] \tag{30}
$$

where C_I is the value of c_f in element I.

Substitution of the expressions from Eqs. (29a), (29b), and (30) into Eq. (17a), we obtain

$$
\begin{aligned}
&-\frac{1}{h_{I-1}}M_{I-1} + \left(\frac{1}{h_{I-1}} + \frac{1}{h_I}\right)M_I - \frac{1}{h_I}M_{I+1} + \frac{1}{8}C_{I-1}h_{I-1}W_{I-1} \\
&+ \frac{3}{8}\left(C_{I-1}h_{I-1} + C_I h_I\right)W_I + \frac{1}{8}C_I h_I W_{I+1} - \frac{\bar{A}_{I-1}\,\Delta W_{I-1}}{h_{I-1}}U_{I-1} \\
&+ \left(\frac{\bar{A}_{I-1}\,\Delta W_{I-1}}{h_{I-1}} + \frac{\bar{A}_I\,\Delta W_I}{h_I}\right)U_I - \frac{\bar{A}_I\,\Delta W_I}{h_I}U_{I+1} - 0.5\frac{\bar{A}_{I-1}\,(\Delta W)^2_{I-1}}{h_{I-1}}W_{I-1} \\
&+ 0.5\left(\frac{\bar{A}_{I-1}\,(\Delta W)^2_{I-1}}{h_{I-1}} + \frac{\bar{A}_I\,(\Delta W)^2_I}{h_I}\right)W_I - 0.5\frac{\bar{A}_I\,(\Delta W)^2_I}{h_I}W_{I+1} - Q_I \\
&+ 0.5\left[\bar{B}_{I-1}\,\Delta W_{I-1}\,M_{I-1} + \left(\bar{B}_{I-1}\,\Delta W_{I-1} - \bar{B}_I\,\Delta W_I\right)M_I - \bar{B}_I\,\Delta W_I\,M_{I+1}\right]
\end{aligned} \tag{31}
$$

For the boundary nodes 1 and $N+1$, we have

$$
\begin{aligned}
0 &= -V_1^{(1)} + \frac{1}{h_1}M_1 - \frac{1}{h_1}M_2 + \frac{3h_1}{8}C_1W_1 + \frac{h_1}{8}C_1W_2 \\
&\quad + \frac{\bar{A}_1\,\Delta W_1}{h_1}\left(U_1 - U_2\right) + 0.5\frac{\bar{A}_1\,(\Delta W)^2_1}{h_1}\left(W_1 - W_2\right) \\
&\quad - 0.5\bar{B}_1\,\Delta W_1\,M_1 - 0.5\bar{B}_1\,\Delta W_1\,M_2 - Q_1
\end{aligned} \tag{32a}
$$

$$
\begin{aligned}
0 &= -V_2^{(N+1)} - \frac{1}{h_N}M_N + \frac{1}{h_N}M_{N+1} + \frac{h_N}{8}C_N W_N + \frac{3h_N}{8}C_N W_{N+1} \\
&\quad + \frac{\bar{A}_N\,\Delta W_N}{h_N}\left(U_{N+1} - U_N\right) + 0.5\frac{\bar{A}_N\,(\Delta W)^2_N}{h_N}\left(W_{N+1} - W_N\right) \\
&\quad + 0.5\bar{B}_N\,\Delta W_N\,M_N + 0.5\bar{B}_N\,\Delta W_N\,M_{N+1} - Q_{N+1}
\end{aligned} \tag{32b}
$$

where

$$
Q_I = \int_{0.5h_{I-1}}^{h_{I-1}} q\,d\bar{x} + \int_0^{h_I} q\,d\bar{x},\quad Q_1 = \int_0^{0.5h_1} q\,d\bar{x},\quad Q_{N+1} = \int_{0.5h_N}^{h_N} q\,d\bar{x}, \tag{33}
$$

Discretization of Eq. (7c)

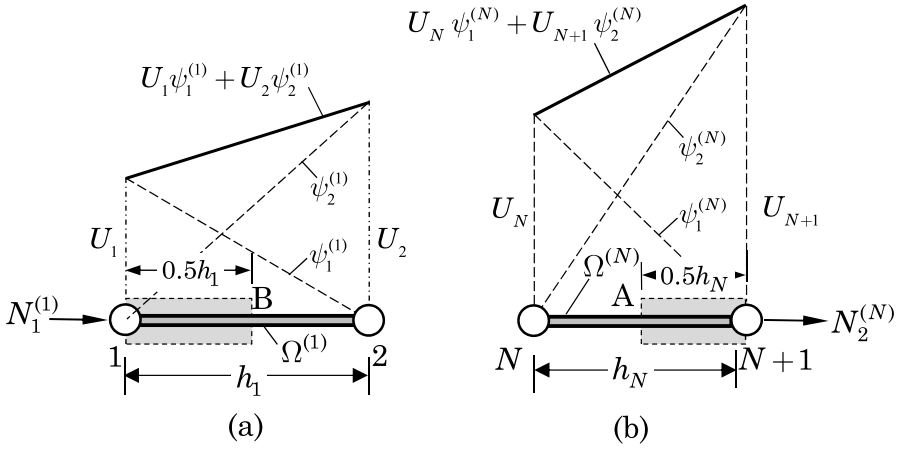

Fig. 6. The (half) finite domains at the boundary nodes.

The discretized equations associated with Eq. (7c) are obtained substituting the following approximations for $\Theta_1^{(I)}$ and $\Theta_2^{(I)}$ and replacing other terms as before,

$$\Theta_1^{(I)} = \frac{W_{I-1} - W_I}{h_{I-1}}, \quad \Theta_2^{(I)} = \frac{W_I - W_{I+1}}{h_I} \tag{34}$$

For an interior node, we obtain

$$\begin{aligned} &-\frac{1}{h_{I-1}}W_{I-1} + \left(\frac{1}{h_{I-1}} + \frac{1}{h_I}\right)W_I - \frac{1}{h_I}W_{I+1} \\ &\quad - \frac{1}{8}\frac{h_{I-1}}{D_{I-1}}M_{I-1} - \frac{3}{8}\left(\frac{h_{I-1}}{D_{I-1}} + \frac{h_I}{D_I}\right)M_I - \frac{1}{8}\frac{h_I}{D_I}M_{I+1} \\ &\quad - 0.5\bar{B}_{I-1}U_{I-1} + 0.5\left(\bar{B}_{I-1} - \bar{B}_I\right)U_I + 0.5\bar{B}_I U_{I+1} \\ &\quad - 0.25\bar{B}_{I-1}\,\Delta W_{I-1}\,W_{I-1} + 0.25\left(\bar{B}_{I-1}\,\Delta W_{I-1} - \bar{B}_I\,\Delta W_I\right)W_I \\ &\quad + 0.25\bar{B}_I\,\Delta W_I\,W_{I+1} = 0 \end{aligned} \tag{35}$$

Here D_I denotes the value of D_{xx} in element I and $\bar{B}_I$ denotes the value of B_{xx}/D_{xx} in element I. For the boundary nodes 1 and $N+1$, we have

$$\begin{aligned} 0 &= -\Theta_1^{(1)} + \frac{1}{h_1}W_1 - \frac{1}{h_1}W_2 - \frac{3}{8}\frac{h_1}{D_1}M_1 - \frac{1}{8}\frac{h_1}{D_1}M_2 \\ &\quad - 0.5\bar{B}_1U_1 + 0.5\bar{B}_1U_2 - 0.25\bar{B}_1\,\Delta W_1\,W_1 + 0.25\bar{B}_1\,\Delta W_1\,W_2 \end{aligned} \tag{36a}$$

$$\begin{aligned} 0 &= \Theta_2^{(N+1)} - \frac{1}{h_N}W_N + \frac{1}{h_N}W_{N+1} - \frac{1}{8}\frac{h_N}{D_N}M_N - \frac{3}{8}\frac{h_N}{D_N}M_{N+1} - 0.5\bar{B}_N U_N \\ &\quad + 0.5\bar{B}_N U_{N+1} - 0.25\bar{B}_N\,\Delta W_N\,W_N + 0.25\bar{B}_N\,\Delta W_N\,W_{N+1} \end{aligned} \tag{36b}$$

This completes the development of the discretized equations based on the DMFDM for the mixed formulation of the Euler–Bernoulli beam theory.

3.2. Timoshenko beams

3.2.1. Displacement model

Following the procedure describe in the previous section, we present discretized equations associated with Eqs. (10a)–(10c), with (N_{xx}, M_{xx}, Q_x) replaced in terms of the displacements using Eqs. (11a)–(11c). Fig. 7 shows the nodal degrees of freedom for the displacement model of the TBT. The integral statements (after the integration-by-parts) of Eqs. (10a)–(10c) are:

$$0 = -N_1^{(I)} - N_2^{(I)} - \int_{x_a^{(I)}}^{x_b^{(I)}} f\,dx \tag{37a}$$

$$0 = -V_1^{(I)} - V_2^{(I)} + \int_{x_a^{(I)}}^{x_b^{(I)}} (c_f w - q)dx \tag{37b}$$

$$0 = -M_1^{(I)} - M_2^{(I)} + \int_{x_a^{(I)}}^{x_b^{(I)}} S_{xz}\left(\phi_x + \frac{dw}{dx}\right)dx \tag{37c}$$

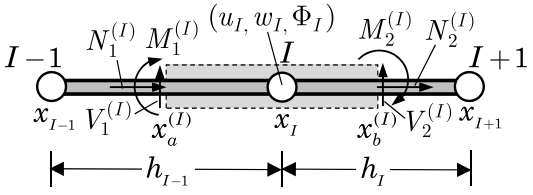

Fig. 7. A typical control domain for the displacement model of the TBT.

where

$$N_1^{(I)} \equiv -\left[A_{xx}\left(\frac{du}{dx} + \tfrac{1}{2}\left(\frac{dw}{dx}\right)^2\right) + B_{xx}\frac{d\phi_x}{dx}\right]_{x_a^{(I)}} \tag{38a}$$

$$N_2^{(I)} \equiv \left[A_{xx}\left(\frac{du}{dx} + \tfrac{1}{2}\left(\frac{dw}{dx}\right)^2\right) + B_{xx}\frac{d\phi_x}{dx}\right]_{x_b^{(I)}} \tag{38b}$$

$$V_1^{(I)} \equiv -\left[S_{xz}\left(\phi_x + \frac{dw}{dx}\right) + N_{xx}\frac{dw}{dx}\right]_{x_a^{(I)}} \tag{38c}$$

$$V_2^{(I)} \equiv \left[S_{xz}\left(\phi_x + \frac{dw}{dx}\right) + N_{xx}\frac{dw}{dx}\right]_{x_b^{(I)}} \tag{38d}$$

$$M_1^{(I)} \equiv -\left[B_{xx}\left(\frac{du}{dx} + \tfrac{1}{2}\left(\frac{dw}{dx}\right)^2\right) + D_{xx}\frac{d\phi_x}{dx}\right]_{x_a^{(I)}} \tag{38e}$$

$$M_2^{(I)} \equiv \left[B_{xx}\left(\frac{du}{dx} + \tfrac{1}{2}\left(\frac{dw}{dx}\right)^2\right) + D_{xx}\frac{d\phi_x}{dx}\right]_{x_b^{(I)}} \tag{38f}$$

The values of $N_i^{(I)}$, $V_i^{(I)}$, and $M_i^{(I)}$ ($i = 1, 2$) in Eqs. (38a)–(38f) can be expressed in terms of the nodal values (U_I, W_I, Φ_I) of ($u(x)$, $w(x)$, $\phi_x(x)$), respectively, as follows:

$$N_1^{(I)} = -A_{I-1}\frac{U_I - U_{I-1}}{h_{I-1}} - \tfrac{1}{2}A_{I-1}\,\Delta W_{I-1}\frac{W_I - W_{I-1}}{h_{I-1}} - B_{I-1}\frac{\Phi_I - \Phi_{I-1}}{h_{I-1}} \tag{39a}$$

$$\begin{aligned} N_2^{(I)} &= A_I\frac{U_{I+1} - U_I}{h_I} + \tfrac{1}{2}A_I\,\Delta W_I\frac{W_{I+1} - W_I}{h_I} + B_I\frac{\Phi_{I+1} - \Phi_I}{h_I} \\ V_1^{(I)} &= -S_{I-1}\left[\frac{\Phi_{I-1} + \Phi_I}{2} + \frac{W_I - W_{I-1}}{h_{I-1}}\right] \end{aligned} \tag{39b}$$

$$V_2^{(I)} = S_I\left[\frac{\Phi_I + \Phi_{I+1}}{2} + \frac{W_{I+1} - W_I}{h_I}\right]$$

$$M_1^{(I)} = -B_{I-1}\frac{U_I - U_{I-1}}{h_{I-1}} - \tfrac{1}{2}B_{I-1}\,\Delta W_{I-1}\frac{W_I - W_{I-1}}{h_{I-1}} - D_{I-1}\frac{\Phi_I - \Phi_{I-1}}{h_{I-1}} \tag{39c}$$

$$M_2^{(I)} = B_I\frac{U_{I+1} - U_I}{h_I} + \tfrac{1}{2}B_I\,\Delta W_I\frac{W_{I+1} - W_I}{h_I} + D_I\frac{\Phi_{I+1} - \Phi_I}{h_I}$$

$$\int_{x_a^{(I)}}^{x_b^{(I)}} S_{xz}\left(\phi_x+\frac{dw}{dx}\right)dx=\tfrac{1}{4}S_{I-1}\left(\Phi_{I-1}+\Phi_I\right)h_{I-1}+\tfrac{1}{4}S_I\left(\Phi_I+\Phi_{I+1}\right)h_I + \tfrac{1}{2}S_{I-1}\left(W_I-W_{I-1}\right)+\tfrac{1}{2}S_I\left(W_{I+1}-W_I\right) \tag{39d}$$

We note that in evaluating the integral in Eq. (39d), ϕ_x is treated as a constant to avoid shear locking.

With the relations in Eqs. (39a)–(39d), Eqs. (37a)–(37c) can be expressed as

$$\begin{aligned}0=&-\frac{A_{I-1}}{h_{I-1}}U_{I-1}+\left(\frac{A_{I-1}}{h_{I-1}}+\frac{A_I}{h_I}\right)U_I-\frac{A_I}{h_I}U_{I+1}+0.5\left[-\frac{A_{I-1}\Delta W_{I-1}}{h_{I-1}}W_{I-1}\right.\\&\left.+\left(\frac{A_{I-1}\Delta W_{I-1}}{h_{I-1}}+\frac{A_I\Delta W_I}{h_I}\right)W_I-\frac{A_I\Delta W_I}{h_I}W_{I+1}\right]\\&-\frac{B_{I-1}}{h_{I-1}}\Phi_{I-1}+\left(\frac{B_{I-1}}{h_{I-1}}+\frac{B_I}{h_I}\right)\Phi_I-\frac{B_I}{h_I}\Phi_{I+1}-F_I\end{aligned} \tag{40a}$$

$$\begin{aligned}0=&-\frac{S_{I-1}}{h_{I-1}}W_{I-1}+\left(\frac{S_{I-1}}{h_{I-1}}+\frac{S_I}{h_I}\right)W_I-\frac{S_I}{h_I}W_{I+1}+0.125C_{I-1}W_{I-1}h_{I-1}\\&+0.375\left(C_{I-1}h_{I-1}+C_Ih_I\right)W_I+0.125C_IW_{I+1}h_I\\&+0.5S_{I-1}\Phi_{I-1}+0.5\left(S_{I-1}-S_I\right)\Phi_I-0.5S_I\Phi_{I+1}-Q_I\end{aligned} \tag{40b}$$

$$\begin{aligned}0=&-\frac{B_{I-1}}{h_{I-1}}U_{I-1}+\left(\frac{B_{I-1}}{h_{I-1}}+\frac{B_I}{h_I}\right)U_I-\frac{B_I}{h_I}U_{I+1}\\&-0.5\frac{B_{I-1}\Delta W_{I-1}}{h_{I-1}}W_{I-1}+0.5\left(\frac{B_{I-1}\Delta W_{I-1}}{h_{I-1}}+\frac{B_I\Delta W_I}{h_I}\right)W_I\\&-0.5\frac{B_I\Delta W_I}{h_I}W_{I+1}-0.5S_{I-1}W_{I-1}+0.5\left(S_{I-1}-S_I\right)W_I+0.5S_IW_{I+1}\\&-\frac{D_{I-1}}{h_{I-1}}\Phi_{I-1}+\left(\frac{D_{I-1}}{h_{I-1}}+\frac{D_I}{h_I}\right)\Phi_I-\frac{D_I}{h_I}\Phi_{I+1}+0.25S_{I-1}h_{I-1}\Phi_{I-1}\\&+0.25\left(S_{I-1}h_{I-1}+S_Ih_I\right)\Phi_I+0.25S_Ih_I\Phi_{I+1}\end{aligned} \tag{40c}$$

Next, we should obtain the discretized equations for the boundary nodes. The discretized equations of the left boundary node are

$$0=-N_1^{(1)}+\frac{A_1}{h_1}\left(U_1-U_2\right)+\frac{B_1}{h_1}\left(\Phi_1-\Phi_2\right)+0.5\frac{A_1\Delta W_1}{h_1}\left(W_1-W_2\right)-F_1 \tag{41a}$$

$$0=-V_1^{(1)}+\frac{S_1}{h_1}\left(W_1-W_2\right)-0.5S_1\left(\Phi_1+\Phi_2\right)+\frac{h_1}{8}C_1\left(3W_1+W_2\right)-Q_1 \tag{41b}$$

$$\begin{aligned}0=&-M_1^{(1)}-\frac{B_1}{h_1}\left(U_2-U_1\right)+0.5S_1(W_2-W_1)-\frac{D_1}{h_1}\left(\Phi_2-\Phi_1\right)\\&+0.25S_1h_1\left(\Phi_1+\Phi_2\right)-0.5\frac{B_1\Delta W_1}{h_1}\left(W_2-W_1\right)\end{aligned} \tag{41c}$$

For the node $N+1$ on the right boundary, we have

$$\begin{aligned}0=&-N_2^{(N+1)}+\frac{A_N}{h_N}\left(U_{N+1}-U_N\right)+\frac{B_N}{h_N}\left(\Phi_{N+1}-\Phi_N\right)\\&+0.5\frac{A_N\Delta W_N}{h_N}\left(W_{N+1}-W_N\right)-F_{N+1}\end{aligned} \tag{42a}$$

$$\begin{aligned}0=&-V_2^{(N+1)}+\frac{S_N}{h_N}\left(W_{N+1}-W_N\right)+\frac{h_N}{8}C_N\left(W_N+3W_{N+1}\right)\\&+0.5S_N(\Phi_{N+1}+\Phi_N)-Q_{N+1}\end{aligned} \tag{42b}$$

$$\begin{aligned}0=&-M_2^{(N+1)}+\frac{B_N}{h_N}\left(U_{N+1}-U_N\right)+0.5S_N(W_{N+1}-W_N)+\frac{D_N}{h_N}\left(\Phi_{N+1}-\Phi_N\right)\\&+0.25S_Nh_N\left(\Phi_N+\Phi_{N+1}\right)+0.5\frac{B_N\Delta W_N}{h_N}\left(W_{N+1}-W_N\right)\end{aligned} \tag{42c}$$

3.3. Mixed model

Lastly, we develop the mixed DMFDM model of Eqs. (13a)–(13c). Due to the close similarity between Eqs. (13a)–(13c) and Eqs. (7a)–(7c), the discretized equations in Eqs. (25), (27), (28), (31), (32a), (32b), (35), (36a), and (36b), are valid here, with the additional contributions to Eqs. (35), (36a), and (36b) due to the expression

$$\left[\frac{1}{S_{xz}}\frac{dM_{xx}}{dx}\right]_{x_a^{(I)}}^{x_b^{(I)}} \tag{43}$$

The additional terms are:

$$\text{Node } I: \quad \frac{1}{h_{I-1}}\frac{1}{S_{I-1}}M_{I-1}-\left(\frac{1}{h_{I-1}}\frac{1}{S_{I-1}}+\frac{1}{h_I}\frac{1}{S_I}\right)M_I+\frac{1}{h_I}\frac{1}{S_I}M_{I+1} \tag{44a}$$

$$\text{Node } 1: \quad \frac{1}{S_1}\frac{M_2-M_1}{h_1} \tag{44b}$$

$$\text{Node } N+1: \quad \frac{1}{S_Nh_N}M_N-\frac{1}{S_Nh_N}M_{N+1} \tag{44c}$$

where S_I is the value of S_{xz} in element $\Omega^{(I)}$.

4. Numerical results

In this section we consider applications of the methodology developed in the preceding sections. Numerical results obtained with the FEM and DMFDM are compared in all cases. We use four beam models of the FEM and three beam models of DMFDM, as designated here:

- **FE-EB(D)** - Displacement finite element model of the EBT
- **FE-EB(M)** - Mixed finite element model of the EBT
- **FE-TB(D)** - Displacement finite element model of the TBT
- **FE-TB(M)** - Mixed finite element model of the TBT
- **DM-EB(M)** - Mixed dual mesh finite domain model of the EBT
- **DM-TB(D)** - Displacement dual mesh finite domain model of the TBT
- **DM-TB(M)** - Mixed dual mesh finite domain model of the TBT

Models **FE-EB(D)** and **FE-TB(D)** can be found in the book by Reddy [2] and they are summarized, along with FE-EB(M) and FE-TB(M) in Appendix for nonlinear FGM beams. The FE-EB(D) model uses Hermite cubic interpolation of $w(x)$ and linear interpolation of $u(x)$, whereas all other elements are based on Lagrange interpolations of all variables. All finite element models other than FE-EB(D) can also use quadratic or higher order interpolations, whereas the dual mesh finite domain formulations presented herein are based on linear interpolations. Thus, for consistency, all numerical results presented herein, with the exception of FE-EB(D), are obtained with linear approximations of all field variables. During the course of this study the required nonlinear finite element models of the FGM beams were also developed to have means to compare the numerical results but the details are not included here as the focus of the present study is on DMFDM.

Here we shall consider a functionally graded beam of length $L=100$ in (254 cm), height $h=1$ in (2.54 cm), and width $b=1$ in (2.54 cm). and subjected to uniformly distributed load of intensity q_0 lb/in (1 lb/in = 175 N/m). The FGM beam is made of two materials with the following values of the moduli, Poisson's ratio, and shear correction coefficient:

$$E_1=30\times10^6 \text{ psi (210 GPa)}, \quad E_2=10\times10^6 \text{ psi (21 GPa)},$$
$$\nu=0.3, \quad K_s=\frac{5}{6}$$

We shall investigate the parametric effects of the power-law index, n and boundary conditions on the transverse deflection and stresses.

Load increments of $\Delta q_0=1.0$ lb/in (175 N/m) and a tolerance of $\epsilon=10^{-3}$ are used in the nonlinear analysis. The initial solution vector is chosen to be $\boldsymbol{\Delta}^0=\mathbf{0}$ so that the first iteration is the linear solution for the first load step. The direct iteration scheme does not converge unless an acceleration parameter, β, is used to evaluate the stiffness matrix, $\mathbf{K}^r=\mathbf{K}(\bar{\boldsymbol{\Delta}}^r)$, at each iteration (see Eq. (22)):

$$\bar{\boldsymbol{\Delta}}^r=(1-\beta)\boldsymbol{\Delta}^r+\beta\boldsymbol{\Delta}^{r-1}, \quad 0\le\beta\le1 \tag{45}$$

where r denotes the iteration number. Thus, using a weighted average of the last two iteration solutions to update the stiffness matrix accelerates the convergence. In the present case, a value of $\beta=0.25--0.35$ is used (after some study with varying β, starting with $\beta=0$).

Linear analysis

We consider functionally graded beams which are either pin-supported at both ends (P–P) or clamped at both ends (C–C). Using the symmetry about $x = L/2$, we use the left half of the beam as the computational domain and investigate the effect of the power-law index on the transverse deflections and bending moments. The boundary conditions on the primarily variables in various models for P–P beams are as follows:

$$\begin{aligned} &\text{Displacement models}: \quad u(0) = w(0) = u(0.5L) = 0, \quad \text{and} \\ &\qquad \frac{dw}{dx}(\tfrac{L}{2}) = 0 \text{ or } \phi(\tfrac{L}{2}) = 0 \\ &\text{Mixed models}: \quad u(0) = w(0) = u(0.5L) = 0, \quad M(0) = 0 \end{aligned} \tag{46}$$

The exact solutions of pinned–pinned functionally graded beams according to the TBT, with the power-law given in Eq. (1), are given by (see [15,16])

$$\begin{aligned} \bar{D}_{xx}\, u(x) &= \frac{q_0 L^3}{12}\left(\xi - 3\xi^2 + 2\xi^3\right) \\ \hat{D}_{xx}\, w(x) &= \frac{q_0 L^4}{24}\left(\xi - 2\xi^3 + \xi^4\right) + \tilde{D}_{xx}\frac{q_0 L^4}{2}\xi(1-\xi) - \hat{B}_{xx}\frac{q_0 L^4}{24}\xi(1-\xi) \end{aligned} \tag{47}$$

$$\begin{aligned} \hat{D}_{xx}\, \phi_x(x) &= -\frac{q_0 L^3}{24}\left(1 - 6\xi^2 + 4\xi^3\right) + \hat{B}_{xx}\frac{q_0 L^3}{24}(1-2\xi) \\ M_{xx}(x) &= \frac{q_0 L^2}{2}\xi(1-\xi), \quad Q_x(x) = \frac{dM_{xx}}{dx} = \frac{q_0 L}{2}(1-2\xi) \end{aligned}$$

where $\xi = x/L$ and

$$\hat{D}_{xx} = \frac{D^*_{xx}}{A_{xx}}, \quad \bar{D}_{xx} = \frac{D^*_{xx}}{B_{xx}}, \quad \hat{B}_{xx} = \frac{B^2_{xx}}{D_{xx}A_{xx}}, \quad \tilde{D}_{xx} = \frac{D^*_{xx}}{A_{xx}S_{xz}} \tag{48}$$

The EBT solutions are obtained from Eq. (47) by setting $\tilde{D}_{xx} = 0$ and replacing ϕ_x with $-dw/dx$. It is interesting to note that the bending moment and shear force for the linear case do not depend on B_{xx}. However, the nonlinear solutions show that the bending moment does depend on B_{xx}.

The boundary conditions on the primary variables in various models for the C–C beams are as follows (replace dw/dx with ϕ_x for the TBT):

$$\begin{aligned} &\text{Displacement models}: \quad u(0) = w(0) = 0, \quad \frac{dw}{dx}(0) = 0, \\ &\qquad u(L/2) = \frac{dw}{dx}(\tfrac{L}{2}) = 0 \\ &\text{Mixed models}: \quad u(0) = w(0) = 0, \quad u(L/2) = 0 \end{aligned} \tag{49}$$

The exact solutions for clamped–clamped beams according to the TBT are given by ($\xi = x/L$)

$$\begin{aligned} \bar{D}_{xx}u(x) &= \frac{q_0 L^3}{12}\left(\xi - 3\xi^2 + 2\xi^3\right) \\ \hat{D}_{xx}w(x) &= \frac{q_0 L^4}{24}\xi^2(1-\xi)^2 + \tilde{D}_{xx}\frac{q_0 L^4}{2}\left(\xi - \xi^2\right) \end{aligned} \tag{50}$$

$$\begin{aligned} \hat{D}_{xx}\phi_x(x) &= -\frac{q_0 L^3}{12}\left(\xi - 3\xi^2 + 2\xi^3\right), \quad M(x) = -\frac{q_0 L^2}{12}\left(1 - 6\xi + 6\xi^2\right) \\ Q_x(x) &= \frac{q_0 L}{2}(1-2\xi) \end{aligned} \tag{51}$$

Extensive numerical studies have been carried out with various models, including mesh independency and value of the acceleration parameter on the convergence, effect of the power-law index, and post-computation of the secondary variables (either the bending moments or the rotations). In all cases, both the DMFDM and FEM models, using 16 linear elements in the half beam, yield results that are indistinguishable in a graphical presentations. Based on the numerical studies, the following observations are made.

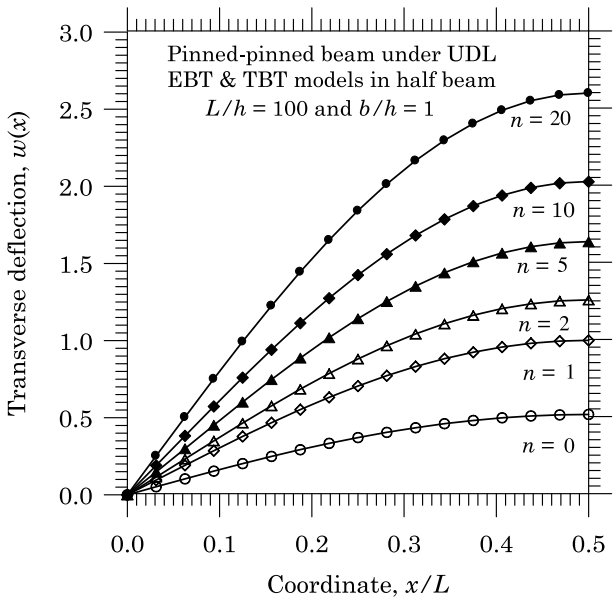

Fig. 8. Linear dimensional deflection w versus $\xi = x/L$ curves for P–P beams. Different power-law index (n) values are used to show its effect on the dimensionless deflection. The solutions predicted by various models of the FEM and DMFDM coincide with each other and with the exact solutions.

(1) The nodal generalized displacements predicted by FE-EB(D) match the exact EBT solutions.
(2) The nodal generalized displacements predicted by FE-TB(D) and DM-TB(D) are the same.
(3) The nodal transverse displacements predicated by FE-EB(D) and FE-EB(M) are the same.
(4) The nodal generalized displacements and post-computed bending moments predicted by FE-TB(D) and DM-TB(D) are identical.
(5) The nodal bending moments predicated by FE-EB(M), FE-TB(M), DM-EB(M), and DM-TB(M) are the same and match the exact solution.
(6) The nodal transverse displacements predicated by FE-TB(M) match the exact TBT solutions.
(7) The post-computed slopes in FE-TB(M), FE-EB(M), DM-EB(M), and DM-TB(M) and the nodal slopes in FE-EB(D) and FE-TB(D) are the same.
(8) The post-computed bending moments in FE-EB(D), FE-TB(D) , FE-EB(M), and FE-TB(M) are the same.

Fig. 8 contains plots of the deflections $w(x)$ predicted for P–P beams by various models as a function of x/L (see [7]). The deflections predicted by all FE and DM models are essentially the same (i.e., the differences cannot be seen in the graph); this also indicates that the effect of shear deformation is negligible (because $L/h = 100$, a thin beam). Similar results are presented for C–C beams (the deflection is not dimensionless) in Fig. 9.

Fig. 10 shows the center deflection w as a function of the power-law index n for the P–P and C–C beams. It is interesting to note that the rate of increase in the deflection has two different regions; the first region has a rapid increase of the deflection while the second region is marked with a slow increase. This is primarily because of the fact that the coupling coefficient B_{xx} varies with n rapidly for the lower values of n followed by a slow decay after $n > 3$.

It is remarkable to see that all of the models yield very accurate solutions for the slope (in mixed models) and bending moment (in displacement models). Fig. 11 show plots of the nodal values and post-computed rotations (ϕ_x or $-dw/dx$) for the C–C beams for three different values of n. The post-computed rotation values fall on the

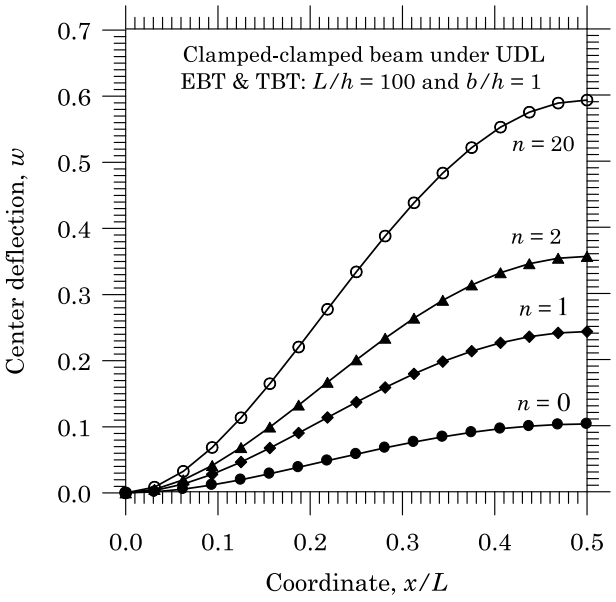

Fig. 9. Linear dimensional deflection w versus $\xi = x/L$ curves for C–C beams. Different power-law index (n) values are used to show its effect on the deflections. The solutions predicted by various models of the FEM and DMFDM coincide with each other and with the exact solutions.

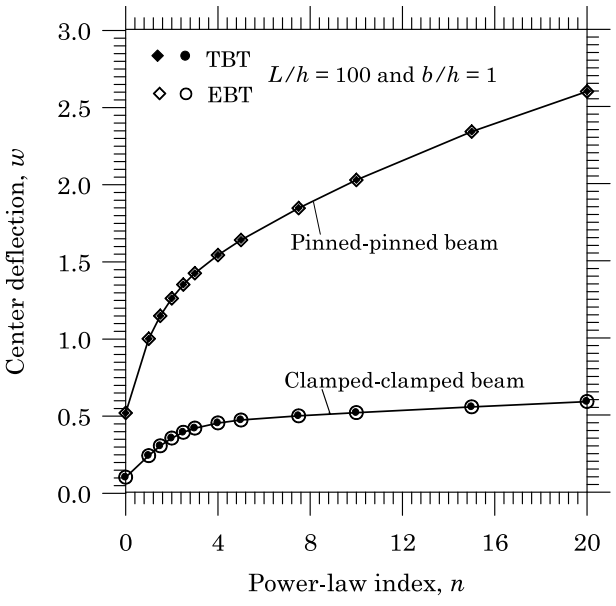

Fig. 10. Linear deflection w versus n curves for C–C and P–P beams. The solutions predicted by various models of the FEM and DMFDM coincide with each other and with the exact solutions, as indicated in the figure.

exact solutions along with the nodal values. Similar behavior is found for the post-computed bending moments (but not reported here) for both types of boundary conditions.

Nonlinear analysis

The nonlinear analysis shows that all models yield solutions that are indistinguishable in the graphs of dimensionless center deflection, $\bar{w} = w(0.5L)\hat{D}_{xx}/L^4$ and bending moment $\bar{M}_{xx} = M_{xx}(0.5)/L^2$ versus the intensity of the uniformly distributed load, q_0. Table 1 contains the results obtained with various models with a uniform mesh of linear approximations of all variables in the half beam (with the direct

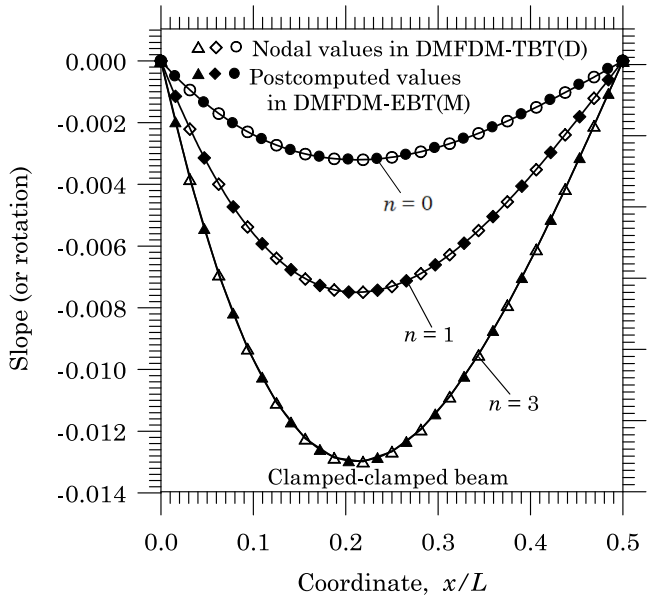

Fig. 11. Linear rotation ($-dw/dx$ or ϕ_x) versus $\xi = x/L$ curves for C–C beams. Different power-law index (n) values are used to show its effect on the rotations. The solutions predicted by various models of the FEM and DMFDM coincide with each other and with the exact solutions.

iteration scheme). Convergence is achieved with different number of iterations for different load steps.

Figs. 12 and 13 contain plots of the center deflection $\bar{w}$ versus q_0 and the center bending moment $\bar{M}_{xx}$ vs. q_0, respectively, for P–P beams and for different values of n. The beams become stiffer as the value of n increases. This is due to the fact that the von Kármán nonlinear strain has stiffening effect through the axial strain, which is quadratically proportional to the gradient of the deflection. As n increases, the beam becomes more flexible and experiences greater bending, which contributes to the stiffening effect. This is similar to the difference between C–C beams and S-S beams, where the S-S beams will exhibit greater effect of the geometric nonlinearity by undergoing larger deflection than a C–C beam. It is interesting to note that the dimensionless bending moment of FGM beams has a cross-over of the bending moment of the homogeneous beam for $n = 1$ with an increase load, although this is not exhibited for $n > 1$. Results for $n > 1$ and $n < 20$ fall between the solutions for $n = 1$ and $n = 20$.

Figs. 14 and 15 contain plots of the center deflection $\bar{w}$ vs. q_0 and the center bending moment $\bar{M}_{xx}$ vs. q_0, respectively, for C–C beams and for different values of n. As in the case of P–P beams, the beams become stiffer but with less rate of increase of nonlinearity because C–C beams are relative stiffer due to the fixed ends. Unlike the P–P beams, the C–C beams do not exhibit the cross over of the bending moment.

5. Closing remarks

In this paper, the dual mesh finite domain method (DMFDM) is introduced as a novel numerical method of solving nonlinear problems, and nonlinear bending of two-constituent through thickness functionally graded Euler–Bernoulli beam theory (EBT) and Timoshenko beam theory (TBT) are used as means. As a part of the present study, mixed (i.e., models that use displacements and moments as nodal degrees of freedom) nonlinear finite element models are also developed. The displacement model of the EBT and displacement and mixed models of the TBT are formulated using the DMFDM. The DMFDM does not suffer from the interelement continuity requirements (of the derivatives) and exact balance of forces as in the FEM, as there is no concept of element

Table 1
Numerical results obtained by various models for the deflections $w(L/2)\times 10$ of a *pinned–pinned* homogeneous beam under a uniformly distributed load. The deflections are given in inches and loads in lb/in.

q_0	FEM				FDM		
	EB(D)	TB(D)	EB(M)	TB(M)	TB(D)	EB(M)	TB(M)
0.5	0.0564	0.0563	0.0564	0.0564	0.0563	0.0563	0.0563 (7)[a]
1	0.0922	0.0921	0.0921	0.0921	0.0921	0.0921	0.0921 (8)
2	0.1364	0.1364	0.1364	0.1364	0.1364	0.1364	0.1364 (13)
3	0.1664	0.1663	0.1664	0.1663	0.1663	0.1663	0.1663 (10)
4	0.1888	0.1888	0.1888	0.1888	0.1888	0.1888	0.1888 (14)
5	0.2078	0.2078	0.2078	0.2078	0.2078	0.2078	0.2078 (14)
6	0.2238	0.2237	0.2237	0.2237	0.2237	0.2237	0.2237 (11)
7	0.2387	0.2386	0.2386	0.2387	0.2386	0.2386	0.2386 (15)
8	0.2117	0.2516	0.2516	0.2516	0.2516	0.2516	0.2516 (15)
9	0.2635	0.2634	0.2634	0.2634	0.2634	0.2634	0.2634 (15)
10	0.2744	0.2743	0.2743	0.2743	0.2743	0.2743	0.2743 (15)
⋮							
20	0.3550 (16)	0.3547 (16)	0.3547 (16)	0.3547 (16)	0.3547 (16)	0.3547 (16)	0.3547(16)

[a]Number of iterations taken to converge (16 linear elements in the half beam); all models took the same number of iterations when the acceleration parameter is taken to be 0.35.

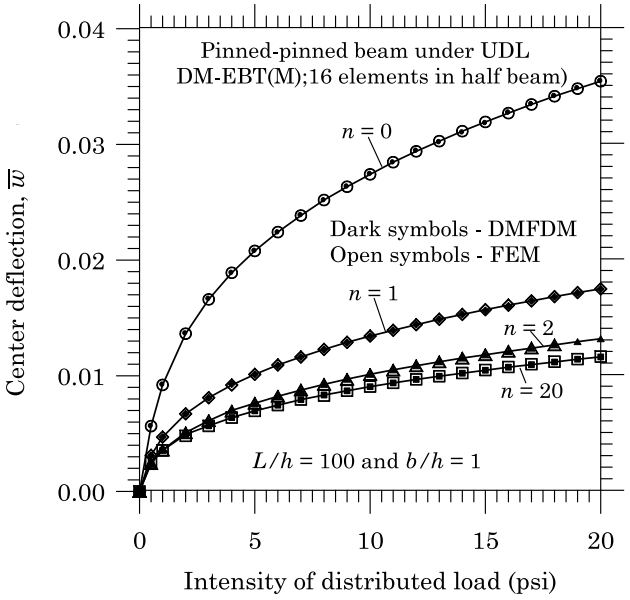

Fig. 12. Nonlinear dimensionless center deflection $\bar{w}$ versus q_0 curves for P–P beams. Different power-law index (n) values are used to show its effect on the deflection. The solutions predicted by various models of the FEM and DMFDM coincide with each other in the graphs.

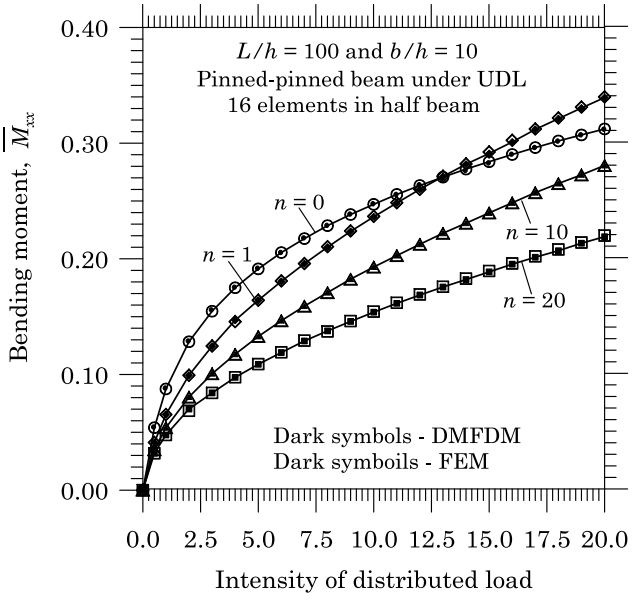

Fig. 13. Nonlinear dimensionless center bending moment $\bar{M}_{xx}$ versus q_0 curves for P–P beams. Different power-law index (n) values are used to show its effect on the rotations. The solutions predicted by various models of the FEM and DMFDM coincide with each other in the graphs.

in the DMFDM. In contrast to the FVM, the DMFDM uses specific approximation of the dependent variables, removing the need for ad-hoc use of Taylor's series to represent the derivatives. Thus, the DMFDM is endowed with the merits of both FEM (interpolation and imposition of physical boundary conditions) and FVM method (satisfaction of the global form of the governing equations and computation of the dual variables).

Numerical results indicate that the DMFDM gives very accurate results, especially for the bending moments. It is found that both FEM and DMFDM have comparable accuracy, but DMFDM has less overhead (formulative steps and computational expense). Although for the one-dimensional problems considered here, this may not be a significant factor, but for multidimensional problems of plates and shells, both stress computation and savings in computational time become significant. Application of the DMFDM to higher-order differential equations requires rewriting them as the first-order or second-order equations, bringing additional unknowns, which are usually physical variables of interest (like stresses or stress resultants). In fact, all equations of mechanics when originally derived are either first order or second order. Only by elimination of the variables (like stresses or stress resultants expressed in terms of displacements), the order goes up.

Extensions of the DMFDM to nonlinear problems of inelasticity and plasticity [17], plates and shells [18], and computational fluid dynamics are expected highlight the advantages of DMFDM over the competing methods like FEM and FVM.

Declaration of competing interest

The authors declare that they have no known competing financial interests or personal relationships that could have appeared to influence the work reported in this paper.

Acknowledgments

The research reported herein, in parts, was supported by the Oscar S. Wyatt Jr. Endowed Chair and projects from Technical Data Analysis (TDA) and the National Science Foundation (NSF Award 1952873) to Texas A&M University. Computational portions of this research were

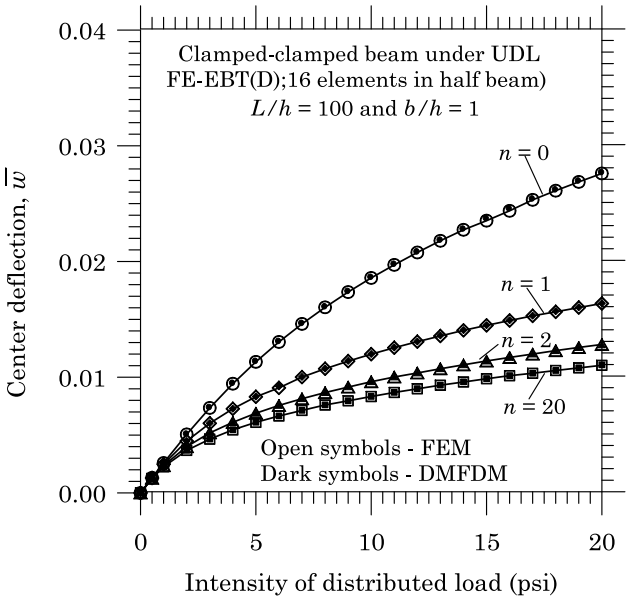

Fig. 14. Nonlinear dimensionless center deflection $\bar{w}$ versus q_0 curves for C–C beams. Different power-law index (n) values are used to show its effect on the deflection. The solutions predicted by various models of the FEM and DMFDM coincide with each other in the graphs.

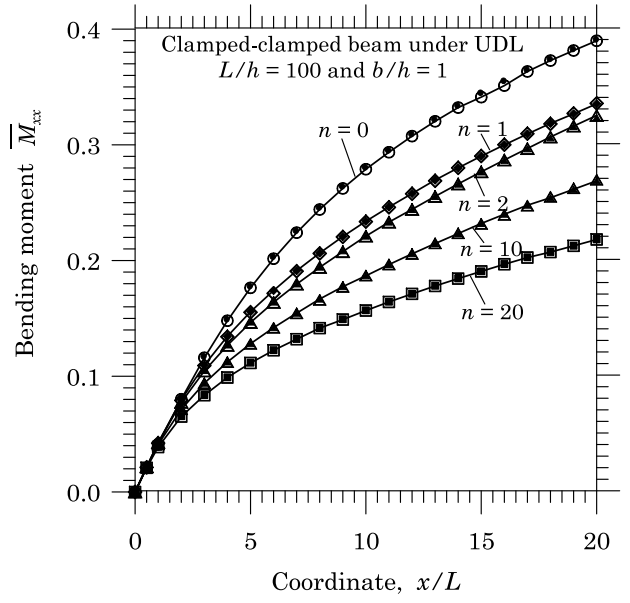

Fig. 15. Nonlinear dimensionless center bending moment $\bar{M}_{xx}$ versus q_0 curves for C–C beams. Different power-law index (n) values are used to show its effect on the rotations. The solutions predicted by various models of the FEM and DMFDM coincide with each other in the graphs.

carried with high performance research computing resources provided by Texas A&M University (https://hprc.tamu.edu).

Appendix. Nonlinear finite element models of FGM beams

The Euler–Bernoulli beam elements

The *displacement finite element model* of the EBT is of the form

$$\begin{bmatrix} \mathbf{K}^{11} & \mathbf{K}^{12} \\ \mathbf{K}^{21} & \mathbf{K}^{22} \end{bmatrix} \begin{Bmatrix} \mathbf{u} \\ \boldsymbol{\Delta} \end{Bmatrix} = \begin{Bmatrix} \mathbf{F}^1 \\ \mathbf{F}^2 \end{Bmatrix} \tag{A.1}$$

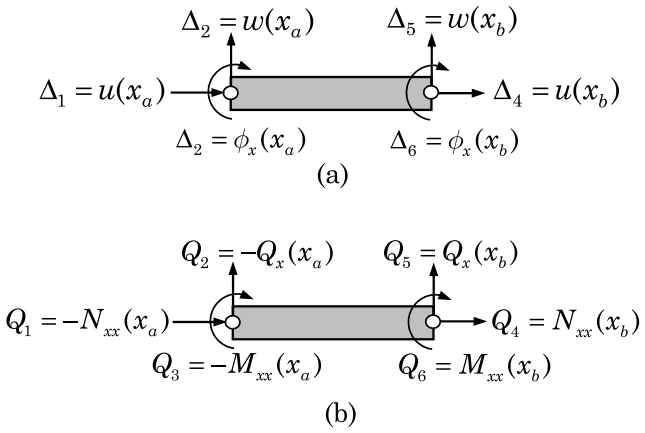

Fig. 16. Generalized nodal forces in the *displacement model* of the EBT.

where

$$\begin{aligned}
K_{ij}^{11} &= \int_{x_a}^{x_b} A_{xx} \frac{d\psi_i}{dx} \frac{d\psi_j}{dx}\, dx, \\
K_{iJ}^{12} &= -\int_{x_a}^{x_b} B_{xx} \frac{d\psi_i}{dx} \frac{d^2\varphi_J}{dx^2}\, dx + \frac{1}{2}\int_{x_a}^{x_b} A_{xx} \frac{dw}{dx} \frac{d\psi_i}{dx} \frac{d\varphi_J}{dx}\, dx \\
F_i^1 &= \psi_i(x_a)\, Q_1 + \psi_i(x_b)\, Q_4 \\
K_{Ij}^{21} &= -\int_{x_a}^{x_b} B_{xx} \frac{d^2\varphi_I}{dx^2} \frac{d\psi_j}{dx}\, dx + \int_{x_a}^{x_b} A_{xx} \frac{dw}{dx} \frac{d\varphi_I}{dx} \frac{d\psi_j}{dx}\, dx \\
K_{IJ}^{22} &= \int_{x_a}^{x_b} \left(D_{xx} \frac{d^2\varphi_I}{dx^2} \frac{d^2\varphi_J}{dx^2} + c_f \varphi_I \varphi_J \right) dx \\
&\quad + \int_{x_a}^{x_b} \left[\frac{1}{2} A_{xx} \left(\frac{dw}{dx} \right)^2 \frac{d\varphi_I}{dx} \frac{d\varphi_J}{dx} \right. \\
&\quad \left. - B_{xx} \frac{dw}{dx} \left(\frac{1}{2} \frac{d^2\varphi_I}{dx^2} \frac{d\varphi_J}{dx} + \frac{d\varphi_I}{dx} \frac{d^2\varphi_J}{dx^2} \right) \right] dx \\
F_I^2 &= \int_{x_a}^{x_b} \varphi_I q\, dx + \varphi_I(x_a)\, Q_2 - \left. \frac{d\varphi_I}{dx} \right|_{x_a} Q_3 + \varphi_I(x_b)\, Q_5 - \left. \frac{d\varphi_I}{dx} \right|_{x_b} Q_6
\end{aligned} \tag{A.2}$$

and Q_i are the generalized nodal forces, as shown in Fig. 16, where replace ϕ_x with $-dw/dx$; φ_I are the Hermite cubic functions and ψ_i are the linear Lagrange interpolation functions; $\mathbf{u}$ denotes the vector of nodal displacements associated with the linear approximation of $u(x)$; and $\boldsymbol{\Delta}$ denotes the nodal displacements (transverse deflection and rotation at each node) associated with the Hermite cubic interpolation of $w(x)$.

The *mixed finite element model* of the EBT, based on the Lagrange interpolation of all variables, is given by

$$\begin{bmatrix} \mathbf{K}^{11} & \mathbf{K}^{12} & \mathbf{K}^{12} \\ \mathbf{K}^{21} & \mathbf{K}^{22} & \mathbf{K}^{23} \\ \mathbf{K}^{31} & \mathbf{K}^{32} & \mathbf{K}^{33} \end{bmatrix} \begin{Bmatrix} \mathbf{u} \\ \mathbf{w} \\ \mathbf{M} \end{Bmatrix} = \begin{Bmatrix} \mathbf{F}^1 \\ \mathbf{F}^2 \\ \mathbf{F}^3 \end{Bmatrix} \tag{A.3}$$

where

$$\begin{aligned}
K_{ij}^{11} &= \int_{x_a}^{x_b} \frac{D_{xx}^*}{D_{xx}} \frac{d\psi_i^{(1)}}{dx} \frac{d\psi_j^{(1)}}{dx}\, dx, \quad F_i^1 = \psi_i^{(1)}(x_a) Q_1 + \psi_i^{(1)}(x_b) Q_4 \\
K_{ij}^{12} &= \frac{1}{2}\int_{x_a}^{x_b} \frac{D_{xx}^*}{D_{xx}} \frac{dw}{dx} \frac{d\psi_i^{(1)}}{dx} \frac{d\psi_j^{(2)}}{dx}\, dx, \quad K_{ij}^{13} = \int_{x_a}^{x_b} \frac{B_{xx}}{D_{xx}} \frac{d\psi_i^{(1)}}{dx} \psi_j^{(3)}\, dx \\
K_{ij}^{21} &= \int_{x_a}^{x_b} \frac{D_{xx}^*}{D_{xx}} \frac{dw}{dx} \frac{d\psi_i^{(2)}}{dx} \frac{d\psi_j^{(1)}}{dx}\, dx \\
K_{ij}^{22} &= \int_{x_a}^{x_b} \left[\frac{1}{2} \frac{D_{xx}^*}{D_{xx}} \left(\frac{dw}{dx} \right)^2 \frac{d\psi_i^{(2)}}{dx} \frac{d\psi_j^{(2)}}{dx} + c_f \psi_i^{(2)} \psi_j^{(2)} \right] dx
\end{aligned}$$

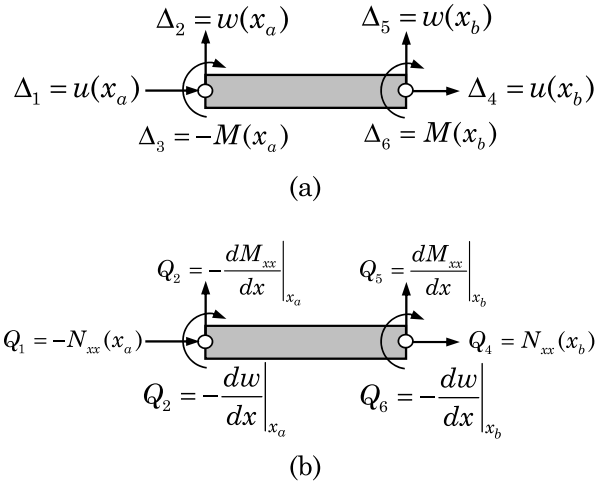

Fig. 17. Generalized nodal forces in the *mixed* model of the EBT.

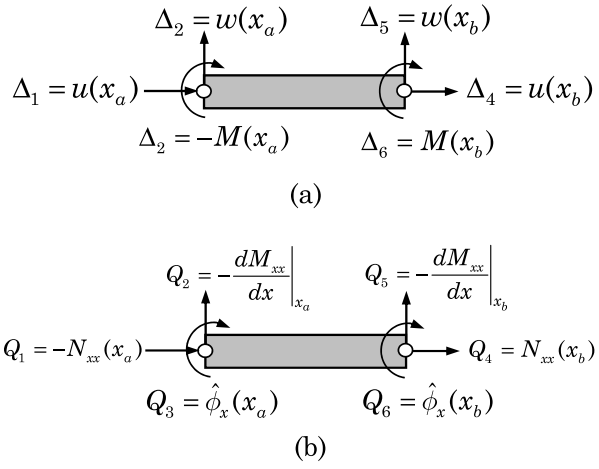

Fig. 18. Generalized nodal forces in the *mixed* model of the EBT.

$$K_{ij}^{23} = \int_{x_a}^{x_b} \left(\frac{d\psi_i^{(2)}}{dx}\frac{d\psi_j^{(3)}}{dx} + \frac{B_{xx}}{D_{xx}}\frac{dw}{dx}\frac{d\psi_i^{(2)}}{dx}\psi_j^{(3)} \right) dx$$

$$F_I^2 = \int_{x_a}^{x_b} \psi_i^{(2)} q\, dx + \psi_i^{(2)}(x_a)Q_2 + \psi_i^{(2)}(x_b)Q_4, \quad K_{ij}^{31} = \int_{x_a}^{x_b} \frac{B_{xx}}{D_{xx}}\psi_i^{(3)}\frac{d\psi_j^{(1)}}{dx}\, dx$$

$$K_{ij}^{32} = \int_{x_a}^{x_b} \left(\frac{d\psi_i^{(3)}}{dx}\frac{d\psi_j^{(2)}}{dx} + \frac{1}{2}\frac{B_{xx}}{D_{xx}}\frac{dw}{dx}\psi_i^{(3)}\frac{d\psi_j^{(2)}}{dx} \right) dx$$

$$K_{ij}^{33} = -\int_{x_a}^{x_b} \frac{1}{D_{xx}}\psi_i^{(3)}\psi_j^{(3)}\, dx, \quad F_I^3 = \psi_i^{(3)}(x_a)Q_3 - \psi_i^{(3)}(x_b)Q_6 \tag{A.4}$$

Here $(\psi_i^{(1)}, \psi_i^{(2)}, \psi_i^{(3)})$ are the Lagrange interpolation functions used for (u, w, M_{xx}), respectively. In general they are different from each other, but here we took them to be the same for all variables (see Fig. 17).

The Timoshenko beam elements

The *displacement finite element model* of the TBT is of the form

$$\begin{bmatrix} \mathbf{K}^{11} & \mathbf{K}^{12} & \mathbf{K}^{13} \\ \mathbf{K}^{21} & \mathbf{K}^{22} & \mathbf{K}^{23} \\ \mathbf{K}^{31} & \mathbf{K}^{32} & \mathbf{K}^{33} \end{bmatrix} \begin{Bmatrix} \mathbf{u} \\ \bar{\mathbf{w}} \\ \mathbf{s} \end{Bmatrix} = \begin{Bmatrix} \mathbf{F}^1 \\ \mathbf{F}^2 \\ \mathbf{F}^3 \end{Bmatrix} \tag{A.5}$$

where (see Fig. 16)

$$K_{ij}^{11} = \int_{x_a}^{x_b} A_{xx}\frac{d\psi_i^{(1)}}{dx}\frac{d\psi_j^{(1)}}{dx}\, dx, \quad K_{ij}^{12} = \frac{1}{2}\int_{x_a}^{x_b} A_{xx}\frac{dw}{dx}\frac{d\psi_i^{(1)}}{dx}\frac{d\psi_j^{(2)}}{dx}\, dx,$$

$$K_{ij}^{13} = \int_{x_a}^{x_b} B_{xx}\frac{d\psi_i^{(1)}}{dx}\frac{d\psi_j^{(3)}}{dx}\, dx, \quad K_{ij}^{21} = \int_{x_a}^{x_b} A_{xx}\frac{dw}{dx}\frac{d\psi_i^{(2)}}{dx}\frac{d\psi_j^{(1)}}{dx}\, dx$$

$$F_i^1 = \int_{x_a}^{x_b} f\psi_i^{(1)}\, dx + \psi_i^{(1)}(x_a)Q_1 + \psi_i^{(1)}(x_b)Q_4$$

$$K_{ij}^{22} = \int_{x_a}^{x_b} \left[S_{xz}\frac{d\psi_i^{(2)}}{dx}\frac{d\psi_j^{(2)}}{dx} + c_f\psi_i^{(2)}\psi_j^{(2)} + \frac{1}{2}A_{xx}\left(\frac{dw}{dx}\right)^2\frac{d\psi_i^{(2)}}{dx}\frac{d\psi_j^{(2)}}{dx} \right] dx$$

$$K_{ij}^{23} = \int_{x_a}^{x_b} \left(S_{xz}\frac{d\psi^{(2)}}{dx}\psi_j^{(3)} + B_{xx}\frac{dw}{dx}\frac{d\psi_i^{(2)}}{dx}\frac{d\psi_j^{(3)}}{dx} \right) dx$$

$$F_i^2 = \int_{x_a}^{x_b} q\psi_i^{(2)}\, dx + \psi_i^{(2)}(x_a)Q_2 + \psi_i^{(2)}(x_b)Q_5$$

$$K_{ij}^{31} = \int_{x_a}^{x_b} B_{xx}\frac{d\psi_i^{(3)}}{dx}\frac{d\psi_j^{(1)}}{dx}\, dx$$

$$K_{ij}^{32} = \int_{x_a}^{x_b} \left(S_{xz}\psi_i^{(3)}\frac{d\psi_j^{(2)}}{dx} + \frac{B_{xx}}{2}\frac{dw}{dx}\frac{d\psi_i^{(3)}}{dx}\frac{d\psi_j^{(2)}}{dx} \right) dx$$

$$K_{ij}^{33} = \int_{x_a}^{x_b} \left(S_{xz}\psi_i^{(3)}\psi_j^{(3)} + D_{xx}\frac{d\psi_i^{(3)}}{dx}\frac{d\psi_j^{(3)}}{dx} \right) dx$$

$$F_i^3 = \psi_i^{(3)}(x_a)Q_3 + \psi_i^{(3)}(x_b)Q_6 \tag{A.6}$$

The *mixed finite element mode* of the TBT has the same form as the mixed finite element model of the EBT, Eq. (A.3), and the coefficients $K_{ij}^{\alpha\beta}$ and F_i^α $(\alpha, \beta = 1, 2, 3)$ also remain the same as those in Eq. (A.4), except for the following coefficient (see Fig. 18):

$$K_{ij}^{33} = -\int_{x_a}^{x_b} \left(\frac{1}{D_{xx}}\psi_i^{(3)}\psi_j^{(3)} + \frac{1}{S_{xz}}\frac{d\psi_i^{(3)}}{dx}\frac{d\psi_j^{(3)}}{dx} \right) dx \tag{A.7}$$

References

[1] J.N. Reddy, An Introduction to the Finite Element Method, fourth ed., McGraw–Hill, New York, NY, 2019.

[2] J.N. Reddy, An Introduction to Nonlinear Finite Element Analysis, second ed., Oxford University Press, Oxford, UK, 2015.

[3] H.K. Versteeg, W. Malalasekera, Computational Fluid Dynamics, The Finite Volume Method, second ed., Pearson Education, Prentice–Hall, Harlow, England, UK, 2007.

[4] J.H. Ferziger, M. Perić, Computational Methods for Fluid Dynamics, third ed., Springer-Verlag, New York, NY, 2002.

[5] S. Mazumder, Numerical methods for partial differential equations, in: Finite Difference and Finite Volume Methods, Elsevier, New York, NY, 2016.

[6] J.N. Reddy, A dual mesh finite domain method for the numerical solution of differential equations, Int. J. Comput. Methods Eng. Sci. Mech. 20 (2019) 212–228.

[7] J.N. Reddy, Praneeth Nampally, A dual mesh finite domain method for the analysis of functionally graded beams, Compos. Struct. 251 (2020) 112648.

[8] J.N. Reddy, Energy Principles and Variational Methods in Applied Mechanics, third ed., John Wiley & Sons, New York, NY, 2018.

[9] J.N. Reddy, A.R. Srinivasa, Non-linear theories of beams and plates accounting for moderate rotations and material length scales, Int. J. Non-Linear Mech. 66 (2014) 43–53.

[10] Y. Obata, N. Noda, T. Tsuji, Steady thermal stresses in a functionally gradient material plate, Trans. Japan Soc. Mech. Eng. 58 (1992) 1689–1695.

[11] G.N. Praveen, J.N. Reddy, Nonlinear transient thermoelastic analysis of functionally graded ceramic-metal plates, Int. J. Solids Struct. 35 (1998) 4457–4476.

[12] J.N. Reddy, Analysis of functionally graded plates, Internat. J. Numer. Methods Engrg. 47 (2000) 663–684.

[13] J.N. Reddy, Sami El-Borgi, Jani Romanoff, Non-linear analysis of functionally graded microbeams using Eringen's nonlocal differential model, Int. J. Non-Linear Mech. 67 (2014) 308–318.

[14] J.N. Reddy, Mechanics of Laminated Composite Plates and Shells: Theory and Analysis, second ed., CRC Press, Boca Raton, Florida, 2004.

[15] C.M. Wang, J.N. Reddy, K.H. Lee, Shear Deformable Beams and Plates, Relationships with Classical Solutions, Elsevier, Amsterdam, 2000.

[16] J.N. Reddy, A. Arbind, Bending relationships between the modified couple stress-based functionally graded Timoshenko beams and homogeneous Bernoulli–Euler beams, Ann. Solid Struct. Mech. 3 (2012) 15–26.

[17] Z. Wang, A.R. Srinivasa, K.R. Rajagopal, J.N. Reddy, Simulation of inextensible elastic–plastic beams based on an implicit rate type model, Int. J. Non-Linear Mech. 99 (2018) 165–172.

[18] J.N. Reddy, Theory and Analysis of Elastic Plates and Shells, second ed., CRC Press, Boca Raton, FL, 2007.